UC San Diego
UC San Diego Previously Published Works

Title

Active-sensing platform for structural health monitoring: Development and deployment

Permalink

https://escholarship.org/uc/item/1sh1c58f

Journal

Structural Health Monitoring, 15(4)

ISSN

Authors

Taylor, Stuart G
Raby, Eric Y
Farinholt, Kevin M
et al.

Publication Date

2016-07-01

DOI

Peer reviewed

Active-sensing Platform for Structural Health Monitoring: Development and Deployment

Journal:	*Structural Health Monitoring*
Manuscript ID:	SHM-15-0019.R1
Manuscript Type:	Original Manuscript
Date Submitted by the Author:	16-Jul-2015
Complete List of Authors:	Taylor, Stuart; Los Alamos National Laboratory, Engineering Institute; University of California, San Diego, Structural Engineering Raby, Eric; Los Alamos National Laboratory, Engineering Institute Farinholt, Kevin; Los Alamos National Laboratory, Engineering Institute Park, Gyuhae; Chonnam National University, Mechanical Engineering Todd, Michael; University of California, San Diego, Dept. of Structural Engineering
Keywords:	embedded sensing, multi-scale sensing, sensor diagnostics, active-sensing, Electro-mechanical impedance
Abstract:	Embedded sensing for structural health monitoring (SHM) is a rapidly expanding field, propelled by algorithmic advances in SHM and the ever-shrinking size and cost of electronic hardware necessary for its implementation. Although commercial systems are available to perform the relevant tasks, they are usually bulky and/or expensive because of their high degree of general utility to a wider range of applications. As a result, multiple separate devices may be required in order to obtain the same results that could be obtained with an SHM-specific device. This work presents the development and deployment of a versatile, wireless active sensing platform (WASP), designed for the particular needs of embedded sensing for multi-scale SHM. The WASP combines a conventional data acquisition ability to record voltage output (e.g. from strain or acceleration transducers) with ultrasonic guided wave-based active sensing, and a seamlessly integrated impedance measurement mode, enabling impedance-based SHM and piezoelectric sensor diagnostics to reduce the potential for false positives in damage identification. The motivation, capabilities, and hardware design for the WASP are reviewed, and three deployment examples are presented, each demonstrating an important aspect of embedded sensing for SHM.

Active-sensing Platform for Structural Health Monitoring: Development and Deployment

Stuart G. Taylor[1], Eric Y. Raby[1], Kevin M. Farinholt[1], Gyuhae Park[2,*], Michael D. Todd[3]

[1] The Engineering Institute
Los Alamos National Laboratory
Los Alamos, NM 87545, USA

[2] School of Mechanical Engineering
Chonnam National University
Gwangju, 505-707, South Korea

[3] Department of Structural Engineering
Jacobs School of Engineering
University of California, San Diego
La Jolla, CA 92093-0085, USA

Embedded sensing for structural health monitoring (SHM) is a rapidly expanding field, propelled by algorithmic advances in SHM and the ever-shrinking size and cost of electronic hardware necessary for its implementation. Although commercial systems are available to perform the relevant tasks, they are usually bulky and/or expensive because of their high degree of general utility to a wider range of applications. As a result, multiple separate devices may be required in order to obtain the same results that could be obtained with an SHM-specific device. This work presents the development and deployment of a versatile, wireless active sensing platform (WASP), designed for the particular needs of embedded sensing for multi-scale SHM. The WASP combines a conventional data acquisition ability to record voltage output (e.g. from strain or acceleration transducers) with ultrasonic guided wave-based active sensing, and a seamlessly integrated impedance measurement mode, enabling impedance-based SHM and piezoelectric sensor diagnostics to reduce the potential for false positives in damage identification. The motivation, capabilities, and hardware design for the WASP are reviewed, and three deployment examples are presented, each demonstrating an important aspect of embedded sensing for SHM.

Index Terms— embedded sensing, sensor diagnostics, multi-scale sensing, active-sensing, Electro-mechanical impedance.

---
* Author to whom correspondence should be addressed: gpark@jnu.ac.kr

I. INTRODUCTION

TECHNOLOGY that enables embedded sensing is becoming more compact, inexpensive, energy efficient, and computationally powerful. As a result, researchers in structural health monitoring (SHM) and related fields have been integrating more sophisticated sensing capabilities into structural assets. Structural health monitoring is distinct from traditional nondestructive evaluation (NDE) in that measurements for SHM are usually made while the structure is in service, precluding many common NDE tools[1]. Typical measurands for SHM include kinematic quantities, such as acceleration, velocity and displacement, as well as force and strain. A wide variety of transducers can be mounted directly to a structure to measure acceleration and force, while velocity and displacement measurements often require external, noncontact methods, and may be better suited to NDE applications than SHM. Strain, which is correlated to structural deflection, can be measured using resistive strain gauges or fiber Bragg gratings. High-frequency strain waves, which can be caused by external impacts, energy release from a propagating crack, or excited as a means of structural interrogation, can be measured using specialized acoustic emissions sensors or piezoelectric materials bonded to a structure's surface. Electromechanical coupling in these materials enables the bidirectional conversion of electrical signals and mechanical response. Measurements for SHM can span frequencies from less than 1 Hz for global vibration modes to greater than 100 kHz for elastic wave propagation.

While some structures can support full-sized, permanently installed data acquisition systems, such as an instrumented bridge, structures with little or no carrying capacity beyond their own self-weight, such as wind turbine rotor blades, demand a compact, lightweight, embedded system. Each embedded system installation brings specific challenges in terms of communications, measurement collection, and system power. Low-power sensor nodes have limited functionality, minimal processing capabilities, and are often intended for use with energy harvesting systems [2,3]. A popular measurement method for low-power sensor nodes[4,5,6] utilizing piezoelectric transducers is the impedance method[7,8] which can be used for sensor diagnostics and to identify local structural damage. In addition to impedance measurements, low-power sensor nodes have been developed and deployed in many different structures, which is well summarized in references[9,10]. Advances in ultrasonic guided wave (UGW)-based methods for SHM have motivated the development of higher power sensor nodes with UGW excitation capability. These nodes have more sophisticated signal conditioning, better onboard processing, and the ability to mechanically excite the structure.

Such devices include the commercially available MD7 node[11] and the SHiMmer active sensing node[12].

Taking advantage of the growing availability of low-power sensors for kinematic measurements, such as <u>Microelectromechanical systems (</u>MEMS<u>)</u> accelerometers, and to better incorporate physics-based models into the SHM process, researchers have also begun developing multi-scale sensor nodes that include acceleration measurement capabilities alongside high-frequency active sensing methods[13],[14]. However, the implementation of such nodes is often piecemeal, with one measurement mode added as an afterthought to the original node's core function. <u>The Wireless Active Sensing Platform (WASP) presented herein has been intentionally designed with an integrated multi-scale sensing functionality, combining a conventional kinematic data acquisition ability with UGW-based active sensing capabilities through the same signal chains. Furthermore, the WASP has a seamlessly integrated impedance measurement mode, enabling impedance-based SHM methods and real-time sensor diagnostics, which can reduce the occurrence of false positives in damage identification.</u> The WASP has also been designed specifically for embedded system deployment, with features including Power over Ethernet, a web-based data acquisition interface, and an interrupt-driven real-time operating system. Its measurement capabilities and deployment features combine to make the WASP an excellent platform for embedded SHM. The authors believe that the development of a device with such capabilities is critical in transitioning the current practice of SHM to field deployment.

II. WASP DESIGN AND METHODOLOGY

A. Overview

The WASP is a multi-scale sensor node, which can acquire simultaneous measurements on any of six channels with a bandwidth from DC to 70 kHz, while providing a synchronized excitation output signal on any non-sensing channel. With an innovative digital switching arrangement, each channel can be used to obtain impedance measurements, deliver a synchronized, power-amplified excitation signal for structural interrogation, or passively monitor a voltage-output transducer. By appropriately configuring each channel's separate input signal chain, the WASP can easily record low-frequency vibration or strain data. These data could then be utilized in concert with a physics-based structural model for state and loads estimation[15]. Combining these estimates with active sensing-based estimates of damage location[14] would enable predictions of future structural performance[16].

The WASP prototype utilizes an ARM Cortex-M3 processor with an STM3210C evaluation board. Two custom printed circuit boards sit atop the evaluation board: an interface "daughter" board and a "mezzanine" board. The daughter board, shown in Fig. 1, provides: (1) physical connectivity for communication between the ARM processor and the analog front end; (2) the data acquisition clock timing control circuitry; and (3) system power conversion from a Power over Ethernet (PoE) source. The mezzanine board, shown in Fig. 2, houses the physical SMA sensor connectors and the analog front end, which contains: (1) the input signal chains with analog-to-digital converter (ADC), (2) the output signal chain with digital-to-analog converter (DAC); and (3) the high-current switches and logic control for measurement mode selection. The major components of the WASP are listed in Table I.
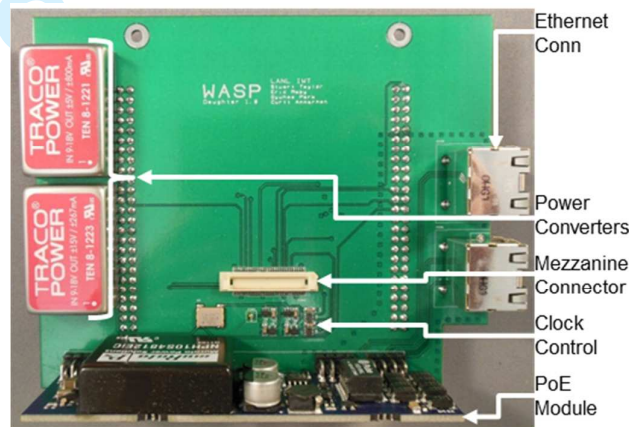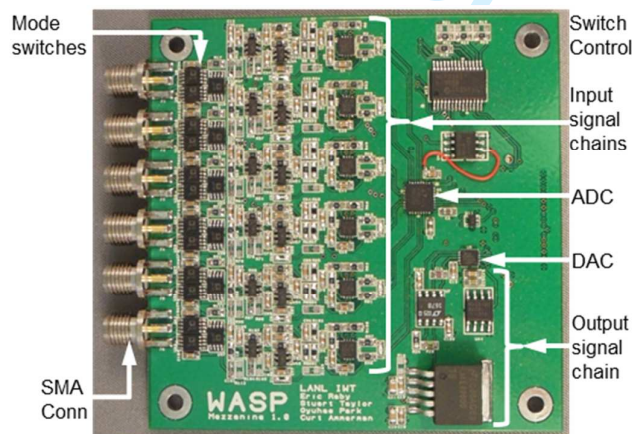

Fig. 1.   WASP daughter board.

Fig. 2.   WASP mezzanine board.

TABLE I: MAJOR COMPONENTS OF THE WASP

Function	Manufacturer	Part No
Development board	ST Microelectronics	STM3210C-EVAL
PoE module	Murata	NMPD0112C
Output switches	Analog Devices	ADG1419
DAC	Linear Technology	LTC2642IDD-16
Voltage amplifier	Linear Technology	LT1678CS8#PBF
Current amplifier	National Semiconductor	LME49600TS-ND
ADC	Linear Technology	LTC2351IUH
Input amplifier	Linear Technology	LT6233IS6
Diff. ADC driver	Linear Technology	LT6350CDD

B. Design

Both power and communications are delivered to the WASP through an Ethernet cable utilizing the IEEE 802.3af Power over Ethernet (PoE) standard. The NMPD0112C PoE module separates 48-Volt AC power from TCP/IP communications and provides a regulated 12V power supply at a maximum of 15W, which is converted to ±15V, ±5V, and ±3V supplies to power both the mezzanine board and the STM3210C. Commands and data are passed between the WASP and a PC through a web-based interface. This method enables the implementation of remote or automated data interrogation. Wireless operation is enabled by use of a Wi-Fi bridge, as was implemented in a flight test on a 20-m rotor diameter wind turbine[17].

A unique arrangement of software-controlled Analog Devices ADG1419 switches enables any of the six channels to be implemented as (1) a measurement channel, (2) an excitation channel, or (3) an impedance measurement circuit. At ± 15V, the switches can carry 215 mA per channel, comparable to the current capacity of the output signal chain. The switch configuration is shown schematically in Fig. 3, and the switch configuration for each mode is given in Table II. In excitation mode, the center pin of the SMA connector is connected to the output signal chain. In response mode, the center pin is connected to the input signal chain. In impedance measurement mode, the output and input signal chains are connected across the SMA connector through the sensor, with the output signal chain on the center pin and the

input signal chain connected to the SMA connector sheath, measuring the voltage across the resistor R_{IMP} to ground.
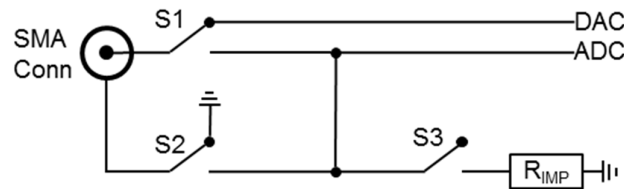

Fig. 3.   Three-mode switch arrangement for WASP sensor connectors.

TABLE II: OPERATIONAL MODES FOR WASP SENSOR CONNECTORS

Operational Mode	Switch Position		
	S1	S2	S3
Excitation	up	up	up
Response	down	up	up
Impedance	up	down	down

The output signal chain is the path for excitation signals in active-sensing and impedance measurement modes. The excitation signals are generated from an LTC2642 DAC, which has a 1 μs settling time, much faster than the WASP's ~70 kHz sampling rate. As a result, the analog signal generated is essentially a stair-step curve, injecting higher frequency content into the excitation signal. In order to mitigate this issue, a single-pole output filter was inserted in the output signal chain prior to amplification. The LT1678 voltage amplifier scales the DAC output to ±15V and feeds the signal to an LME49600 high-current audio buffer that provides up to 250 mA per rail at ±15V.   The output power is sufficient to implement UGW SHM methods only in metallic structures. In order to efficiently use for highly damped structure like composite plate, external amplification is still required, which is the limitation of the current version. The input signal chain is the path for measured signals in all modes. Each of the 6 input channels is an individually configurable 5th-order low-pass Bessel filter with multiple feedback topology, along with two optional single-pole RC filters. These single-pole stages can be implemented as high-pass filters to produce a band-pass filter, or as low-pass filters to improve filter roll-off. Alternatively, two resistors could be utilized to implement a voltage divider, which is sometimes necessary to avoid saturating the ADC when measuring DC-biased signals. Individual input filter chain configurability enables the WASP to function as a self-contained multi-scale SHM system. Each input signal chain is

sampled simultaneously by the 14-bit LTC2351 ADC over ±1.25 Volts. The ADC samples and holds all six channels simultaneously, and then reads the values into memory between samples. This process, along with the output signal synchronization, limits the WASP's bandwidth to ~70 kHz.

C. Impedance Measurements

Sensor diagnostics for piezoelectric transducers utilize impedance measurements to ascertain the health of the sensor and its bond condition[8]. The impedance method relies on the electromechanical nature of piezoelectric transducers in which the material's electrical response is coupled with a structure's mechanical response. The electrical impedance of a piezoelectric patch bonded to a structure will be a function of both the patch's and the structure's mechanical impedance, in addition to the patch's electrical impedance.

In the simplest case, impedance can be measured by applying Ohm's Law with a voltmeter and an ammeter each measuring magnitude and phase. However, because it requires a complex current measurement, this method is rarely implemented. The method implemented in commercial devices (e.g. Agilent's 4294A and Analog Device's AD5933 IC) is the auto-balancing bridge method shown in Fig. 4. This method utilizes an operational amplifier as a current-to-voltage converter to estimate the impedance as

$$Z(\omega) = R \frac{V_{IN}(\omega)}{V_{OUT}(\omega)}. \tag{1}$$
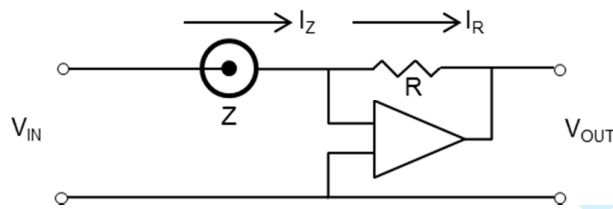

Fig. 4.   Auto-balancing bridge impedance measurement circuit.

The impedance measurement circuit implemented on the WASP is shown in Fig. 5. The measurement circuit input voltage is V_{DAC}, which is not measured but assumed to be the DAC output signal ranging over ±15V. The impedance circuit output voltage is V_{INT}, which enters the WASP's input signal chain. The voltage read by the ADC is V_{ADC}. For the purpose of impedance measurements, the WASP's input signal chain is modeled generically in the complex impedances Z_1 and Z_2. The WASP measurement circuit transfer function (TF) is estimated using Ohm's and Kirchhoff's laws as

$$\frac{V_{INT}(\omega)}{V_{DAC}(\omega)} = \frac{R_{IMP}}{Z(\omega) + R_{IMP}}. \tag{2}$$

The quantity of interest in piezoelectric sensor diagnostics is the admittance, which would be estimated from Eq. (2) as

$$Y(\omega) = \left(R_{IMP} \left(\frac{V_{DAC}(\omega)}{V_{INT}(\omega)} - 1 \right) \right)^{-1}. \tag{3}$$

To estimate V_{INT}, a TF estimate of $V_{ADC}(\omega)/V_{INT}(\omega)$ must be available. In order to obtain this estimate, the response of the total measurement circuit to a white noise excitation signal was recorded for a 50 Ω resistance. Given $R_{IMP} = 100$ and $Z = 50$, V_{INT} was estimated using Eq. (2) as $V_{INT} = \frac{2}{3}V_{DAC}$. Then, the WASP analog front-end TF estimate is

$$TF_{WASP}(\omega) = \frac{V_{ADC}(\omega)}{V_{INT}(\omega)} \approx \frac{3}{2} \left(\frac{V_{ADC}(\omega)}{V_{DAC}(\omega)} \bigg|_{Z=50} \right). \tag{4}$$

From Eqs. (3) and (4), the transducer admittance estimates is

$$Y(\omega) = \left(R \left(\frac{V_{DAC}(\omega)}{V_{ADC}(\omega)} TF_{WASP}(\omega) - 1 \right) \right)^{-1}. \tag{5}$$

Although this work emphasizes impedance measurements for sensor diagnostics purposes, the techniques described here have also been applied for structural damage identification, and those techniques could be implemented together with impedance measurements by the WASP.
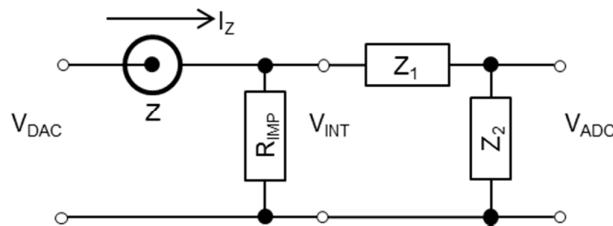

Fig. 5.   Ground-resistor impedance measurement circuit with simplified measurement system model, as implemented in the WASP.

Table III summarizes the WASP specification in all three sensing modes.

TABLE III: Spefication of WASP in three sensing modes

Modes	Sensing frequency range	Maximum Input voltage	ADC	Output
Active-sensing	Up to 70 kHz	±1.25 V	14 bit	± 15 V at 215 mA per channel upto 1 MHz
Impedance-sensing				
Acceleration-sensing				ICP enable

III. EXPERIMENTAL DEMONSTRATIONS

A. Active Sensing

The WASP was deployed on a CX-100 wind turbine rotor blade in a fatigue test as part of an investigation of active-sensing methods for SHM. The 9-m long CX-100 rotor blade, designed by researchers at Sandia National Laboratory (SNL)[18], was an experimental rotor blade with a carbon fiber spar cap and a fiberglass shell over a balsa wood frame. The rotor blade was mounted to approximate a fixed-free boundary condition, and loads were introduced to the blade using a resonant excitation system. The fatigue test ran intermittently for approximately 8.5 million cycles until a fatigue crack became visible. Although the crack that surfaced was obvious under visual inspection and in terms of its impact on the blade's dynamics, the incipient damage, which was not obvious in either of those two modes, was first detectable around 6 million cycles[19],[20].

The surface of the rotor blade was instrumented with active sensing arrays composed of APC International (D-0.500-0.020-851) Piezoelectric (PZT) transducers. Two sensor arrays were monitored by WASPs. Details of the test setup can be found in[19]. Because the WASP's firmware was still in development at the start of the test, it was limited for this test to a 50 kHz sampling rate. One WASP monitored an array on the low-pressure (LP) side of the rotor blade, while the other monitored an array on the high-pressure (HP) side, each in the rotor blade's transitional root area. The array on the low pressure side had transducers located directly over the crack as it surfaced, and these sensors failed as the crack grew. Sensor failure induced by structural failure is outside the scope of this work, so the results from the WASP monitoring the HP side will be presented here. Although the sensor paths on the HP side were not located near the crack, previous results showed that at these lower frequencies (50 kHz vs. 200 kHz), there is general sensitivity to underlying structural changes[21].

The WASP excited a centrally located patch with a chirp signal from 5 kHz to 25 kHz, effectively exciting a diffuse wave field (DWF). Each subsequent measurement was uncorrelated because of the DWF's complex, random nature, precluding the implementation of traditional baseline subtraction methods[22] for UGW signals. As such, data from the WASP were processed to obtain a "local" impulse response from each measurement: a frequency response function (FRF) was estimated for each input-output pair, and that FRF was then inverted to obtain an impulse response function (IRF) estimate. Each estimated IRF was then processed to compute a test statistic for detection purposes. In this case, the Normalized Impulse Residual Energy (NIRE)[21] test statistic was computed as the energy ratio of a given signal envelope to that of an optimal baseline signal[23]. Given the test statistics and knowledge of the true state of the system, an empirical receiver operating characteristic (ROC) curve[24] can be generated, plotting the true detection rate versus the false positive rate for a range of thresholds. The maximum ROC area under the curve (AUC) is 1, and an AUC of 0.5 is equivalent to a random guess. In this case, knowledge of the true state is effectively a "demarcation date" at which the incipient crack became detectable. This date could be obtained independently through some NDE technique, or estimated through a detection optimization process[17]. In this work, the demarcation was taken to be at 6 million cycles (10/21/2011). The NIRE test statistics for the WASP are plotted for each sensor path versus test date in Fig. 6, and the corresponding ROC curves are shown in Fig. 7. The WASP demonstrates a strong ability to detect the incipient damage, with an average AUC of 0.987.
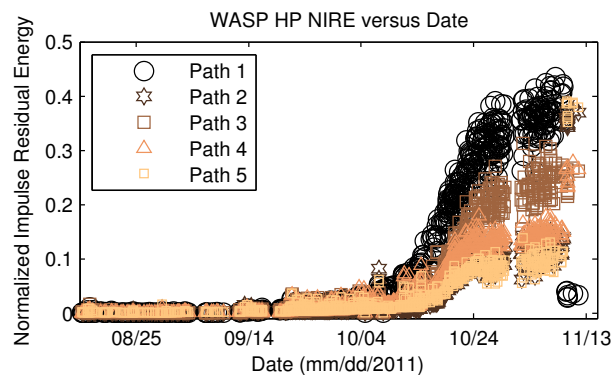

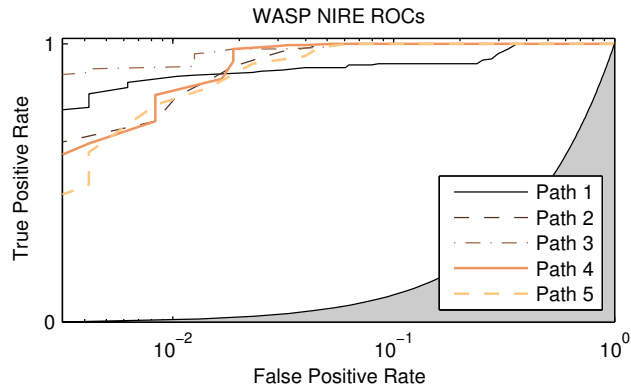Fig. 6.   Raw NIRE test statistics by path for WASP data.

Fig. 7.   ROC curves by path for the NIRE test statistic with WASP data.

For comparison, the ROC curves for the normalized residual energy (NRE) [21,24] test statistic using the commercially available MD7 node[11] with 50 kHz UGW data are shown in Fig. 8. The performance for path 3 is poor because that patch failed very early in the test. The results with the MD7 node indicate a strong ability to detect the incipient damage (on par with the WASP), with an average AUC (excluding path 3) of 0.986.
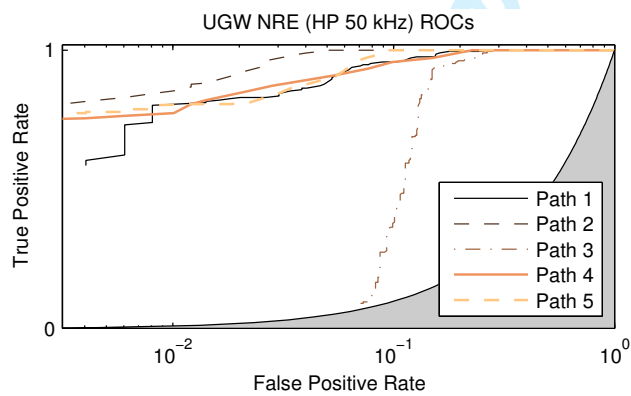

Fig. 8.   ROC curves by path for the NRE test statistic with 50 kHz UGW data.

B. Sensor Diagnostics

In order to demonstrate the WASP's general impedance measurement capability, impedance data were collected for a 50 Ω resistor, a 100 Ω resistor, and a 47 nF capacitor. The excitation was a normally distributed sequence 8050 points long at the maximum sample rate of ~140 kHz. Each transfer function estimate was obtained using the H1 estimator (the ratio of the cross power spectrum and input auto power spectrum) with Welch's method of averaged periodograms[25] using 1024 points, 50% overlap and a Kaiser-Bessel window with β=7.85. The component validation results are shown in Fig. 9, in which the real and imaginary parts of admittance are plotted versus frequency. The WASP impedance measurement circuit breaks down at very low frequencies (below 2 kHz), but otherwise

correctly returns the real admittance values for the 50 Ω and 100 Ω resistors as 20 mΩ^{-1} and 10 mΩ^{-1}, respectively. The measured susceptance for the capacitor increases linearly to ~30 kHz, and then returns to zero at the top of the WASP's 70 kHz bandwidth; this result is caused by measurement system dynamics and the impossibility of measuring both magnitude and phase at the Nyquist limit. The slope of the linear portion of the capacitor susceptance corresponds to a capacitance of 47.3 nF, less than 1% deviation from the nominal value.
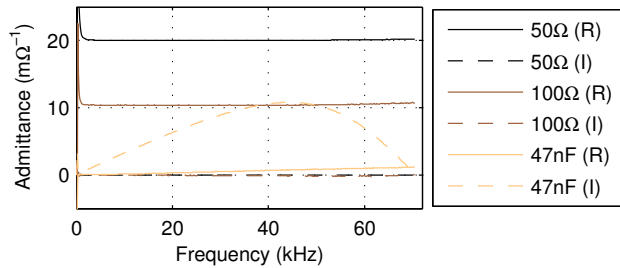
Fig. 9.   WASP admittance measurements for component validation.

The WASP's impedance measurement functionality was demonstrated for sensor diagnostics purposes using an aluminum plate with piezoelectric transducers bonded to its surface. The plate, shown in Fig. 12, has 12 APC International D-0.500-0.020-851 PZT patches. Six patches were mounted according to standard procedures, bonded using a chemical adhesive. Of the six healthy patches, two had been destroyed as part of a previous experiment, so results are presented here for the four remaining ones. Three of the transducers were mounted to simulate progressive debonding, with segments of wax paper placed under nominally 1/4, 1/2 and 3/4 of the patch surface, respectively. The last three transducers were mounted to simulate broken sensors; they were first mounted according to standard procedures, and then cut with a rotary cutting tool to remove nominally 1/4, 1/2 and 3/4 of each patch, respectively.

Data were collected from the debonded and broken patches, and the susceptance slopes (the capacitance) were compared with the average slopes for the healthy patches to determine the relative severity of the defects. The sensor diagnostics results using the WASP are summarized in Table IV, and the susceptance data are plotted for the debonded (D) and broken patches in Fig. 10 and Fig. 11, respectively, along with data for the healthy (H) patches. Although the extent of the susceptance slope changes is greater for the broken patches than for the debonded ones, in each case there is a clearly observable trend indicating the relative severity of the defect using measurements obtained with the WASP. These results

demonstrate the WASP's ability to perform sensor diagnostics measurements while deployed for active sensing SHM.

TABLE IV

MEASURED RELATIVE SUSCEPTANCE SLOPES

Debonded Sensors		Broken Sensors	
Capacitance (nF)	% Change	Capacitance (nF)	% Change
3.75	3.9%	3.18	-11.7%
4.16	15.5%	2.00	-44.6%
4.46	23.6%	1.08	-70.0%
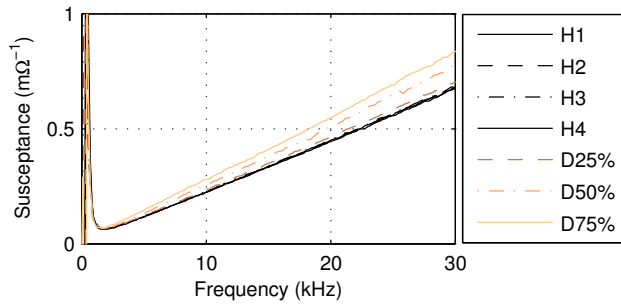
Fig. 10.   WASP susceptance measurements for debonded PZT patches.
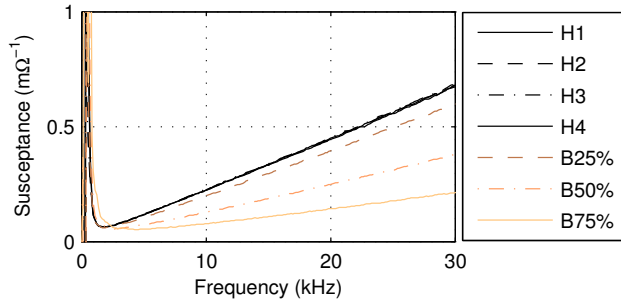
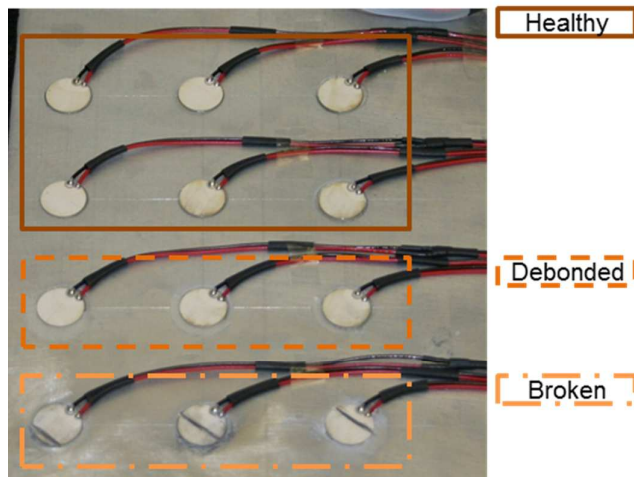Fig. 11.   WASP susceptance measurements for broken PZT patches.

Fig. 12.   Diagnostics test plate with healthy, debonded, and broken sensors.

C. Vibration Monitoring

In a data-driven example of low-frequency vibration monitoring for SHM, the WASP was deployed to monitor the drive system of an astronomical telescope mount. The RAPid Telescopes for Optical Response (RAPTOR) observatory network is made up of several autonomous observatories that search the night sky for astrophysical transients[26]. Each telescope is operated by DC motors driving capstans to actuate two main drive wheels through a friction interface. The capstans are stainless steel rods 8.6 cm long, 6.35 mm in diameter, with a urethane coating. This coating wears with use, ultimately resulting in the inability to control the telescope optics. Examples of capstans are shown in Fig. 13. In a preliminary study, acceleration measurements collected in the in-plane direction with the main drive wheel were shown to be useful in determining the damage state of the capstans[27]. Following those results, a WASP was deployed to monitor a RAPTOR telescope drive system. It records the acceleration signal from a Rieker B1 DC accelerometer affixed to the motor mount. An 8050-point sequence is recorded at 2 kHz each time the telescope moves through its homing sequence. The 110 mV/g DC accelerometer has a range of ±3g and a nominal voltage offset of 2.5 V. The Rieker B1 was chosen in part because it does not require ICP™ signal conditioning, but requires only a regulated DC supply that the WASP can easily provide. Because of the voltage offset, the input signal chain for the accelerometer channel was implemented with a voltage divider to prevent saturating the ADC. Data are automatically downloaded from the WASP and sent off-site for further analysis.

Fig. 13.   RAPTOR telescope drive system capstan examples.

In the telescope drive system, the main drive wheels, which directly contact the capstans, are often marred with slight imperfections in the interface surface. As the capstan drives the wheel, these imperfections inject an impulse train through the interface, allowing the excitation to be modeled as a white noise input, so that the measured acceleration can be modeled as an auto-regressive (AR) process[28]. AR models are a straightforward means of describing time-history data, and because the AR coefficients represent the poles of the structure, they are sensitive to changes in the structure's dynamic characteristics. Utilizing the AR coefficients as a multivariate classification feature set, the Mahalanobis Squared Distance (MSD) can be employed to quantify the similarity (or difference) between a training data set and a data set from an unknown system state. Given a feature vector $\underline{x}$, the MSD is computed as

$$MSD = \left(\underline{x} - \underline{\mu}\right)^T \Sigma^{-1} \left(\underline{x} - \underline{\mu}\right), \qquad\qquad (6)$$

where $\underline{\mu}$ and Σ are the training data mean vector and covariance matrix, respectively. Utilizing the MSD, the detection problem reduces to the application of a threshold to the scalar values, where exceeding that threshold represents a deviation of a given feature vector from the mean system behavior.

For acceleration data collected with the WASP, the power spectral density (PSD) averaged over approximately two months' worth of data is shown in Fig. 14. The PSD was estimated using Welch's method with 1000-point sequences, 50% overlap, and a Kaiser-Bessel window with β=7.85. Each sub-sequence was fit to an AR model of order 18 (determined by inspection of the PSD estimate). Assigning every third sub-sequence for the first half of the total data set as training data, the MSD metric was computed for each sub-sequence. The MSD values are plotted versus test date in Fig. 15. The only observed deviation from the baseline behavior occurred on the night of 11/11/2012, when the temperature at the telescope location dropped by 10° C below the overnight lows thus far experienced for the training data. On this night, three separate measurements were obtained as the telescope periodically

repeated its homing sequence as a result of the capstan's poor performance at low temperature. However, this large excursion could be removed by including some of those points as training data. By incorporating a wider range of operating conditions into the training data, future excursions would be more likely to indicate capstan failure.
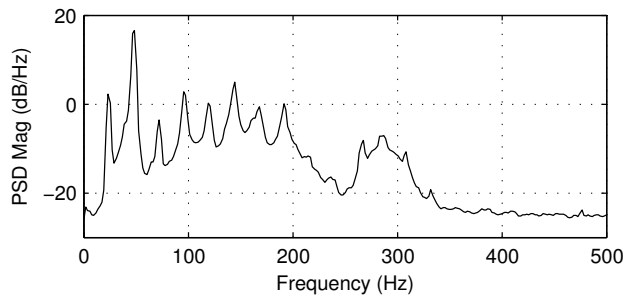

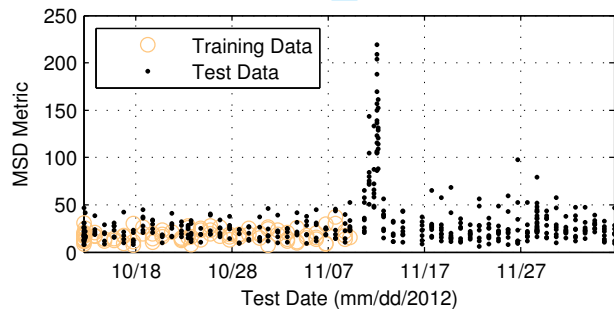Fig. 14.   PSD estimate for motor mount vibration data collected using WASP.

Fig. 15.   MSD metrics versus test date.

IV. DISCUSSION

The multi-scale SHM hardware WASP was presented in this study and demonstrated in three key application areas. First, its ability to collect active-sensing data for SHM was demonstrated in comparison to a commercially available module for UGW measurements, showing a comparable capability to the commercial system in detecting incipient crack development in a 9-m wind turbine rotor blade fatigue test. Second, its ability to collect impedance measurements for piezoelectric sensor diagnostics was demonstrated using experimental examples of debonded and broken piezoelectric patches. Third, its ability to collect vibration measurements for model-based SHM was demonstrated using the acceleration response from a telescope drive system. These capabilities will prove useful in an ongoing manner for in situ monitoring of the health of engineering systems, aiding in the transition of the current practice in SHM to real-world field deployment. The Authors believe that this sensing design scheme could be useful and utilized for other hardware development for SHM applications.

Several research issues remain to be addressed before fully deploying the WASP in long-term SHM applications. First, the ruggedness of WASP must be improved. Although this platform has survived a 3-week deployment on a 20-m rotor diameter wind turbine, embedded systems for SHM must remain operational for long periods of their host structure's service life; the long-term reliability of the WASP under harsh operational and environmental conditions, including vibration and shock tolerance, and the electromagnetic interface (EMI) sensitivity, has yet to be demonstrated. Secondly, several components of WASP are still on the evaluation boards along with original display components with the overall dimensions of 100x100x150 mm. The dimension could be significantly reduced if all the components are integrated into a single printed circuit board. In addition, the WASP has great potential for power management optimization. Although it was designed primarily for its SHM capabilities, the WASP's unique design should be incorporated into a low-power host for its central ARM processor, enabling the platform to be combined with multi-source energy harvesters and mobile power delivery in deployed operation. Furthermore, to truly realize the embedded solution for SHM applications, the signal processing and damage classification algorithms should be embedded within WASP. This process will be also useful to assess the overall computational power requirements for given SHM applications. Authors are currently embedding several classification algorithms, which be the subject for the subsequent papers.

V. CONCLUSION

A unique, multi-scale and versatile wireless active sensing platform (WASP) was developed for application to various aspects of structural health monitoring (SHM). The WASP combines a conventional data acquisition ability to record voltage output (e.g. from strain or acceleration transducers) with ultrasonic guided wave (UGW)-based active sensing capabilities, and a seamlessly integrated impedance measurement mode both for impedance-based SHM and for sensor diagnostics, reducing the potential for false positives in damage identification that plagues standalone active-sensing implementations. We have successfully demonstrated that the WASP can accommodate multiple sensing modalities, making it an excellent platform for active-sensing SHM.

REFERENCES

1. Farrar CR Worden, K An introduction to structural health monitoring, *Proceedings of the Royal Society A Mathematical Physical and Engineering Sciences,* 2007; 365(1851): 303-315.

2. Ni, YQ, Wang, BS, Ko, JM Simulation studies of damage location in Tsing Ma Bridge deck, *SPIE 2000; 3995(312-323).*

3. Anton, SR Sodano, HA, A review of power harvesting using piezoelectric materials (2003–2006), *Smart Materials and Structures,* 2007; 16(3): R1.

4. Mascarenas, DL, Todd, MD, Park, G, Farrar, CR, Development of an impedance-based wireless sensor node for structural health monitoring, *Smart Materials and Structures,* 2007; 16 (6), 2137.

5. Taylor, SG, Farinholt, KM, Park, G, Todd, MD, Farrar, CR, Multi-scale wireless sensor node for health monitoring of civil infrastructure and mechanical systems, *Smart Structures and Systems,* 2010; 6(5-6): 661-673.

6. Min, J, Park, S,   Yun, CB, Song, B, Development of multi-functional wireless impedance sensor nodes for structural health monitoring, *Smart Structures and Systems,* 2010; 6(5-6): 689-709.

7. Park, G, Sohn, H, Farrar, CR, Inman, DJ, Overview of Piezoelectric Impedance-Based Health Monitoring and Path Forward, *Shock & Vibration Digest,* 2003; 35 (6): 451-463.

8. Park, G, Farrar, CR, Rutherford, AC, Robertson, AN, Piezoelectric Active Sensor Self-Diagnostics Using Electrical Admittance Measurements, *Journal of Vibration and Acoustics,* 2006; 128(4): 469-476.

9. Lynch, JP, Loh, KJ, A summary review of wireless sensors and sensor networks for structural health monitoring, *The Shock and Vibration Digest*, 2006; 38(2), 91–128.

10. Overly, TG, Park, G, Farinholt, KM, Farrar, CR, Piezoelectric Active-Sensor Diagnostics and Validation Using Instantaneous Baseline Data, IEEE *Sensors Journal,* 2009; 9(11), 1414-1421.

11. Kessler, SS, Dunn, CT, Borgen, M, Raghavan, A, Duce, J, Banks, DL, A Cable-Free Digital Sensor-Bus for Structural Health Monitoring of Large Area Composite Structures, Proceedings of the Annual Conference of the Prognostics and Health Management Society, 2009.

12. Musiani, D, Lin, K, Rosing, TS, Active sensing platform for wireless structural health monitoring, Proceedings of the 6th international conference on Information processing in sensor networks, Cambridge, Massachusetts, USA, 2007.

13. Ho, DD, Nguyen, KD, Yoon, HS, Kim, JT, Multiscale Acceleration-Dynamic Strain-Impedance Sensor System for Structural Health Monitoring, *International Journal of Distributed Sensor Networks,* vol. 2012, p. 17.

14. Flynn, EB, Todd, MD, Wilcox, PD, Drinkwater, BW, Croxford, AJ, Maximum-likelihood estimation of damage location in guided-wave structural health monitoring, *Proceedings of the Royal Society A Mathematical Physical and Engineering Sciences,* 2011; 467(2133): 2575-2596.

15. Hernandez, A, Swartz, RA, Zimmerman, A, A Framework for Embedded Load Estimation from Structural Response of Wind Turbines, in *Rotating Machinery, Structural Health Monitoring, Shock and Vibration, Volume 5*. vol. 8, T. Proulx, Ed., ed: Springer New York, 2011, pp. 295-305.

16. Gobbato, M, Conte, JP, Kosmatka, JB, Farrar, CR, A reliability-based framework for fatigue damage prognosis of composite aircraft structures, *Probabilistic Engineering Mechanics,* 2012; 29: 176-188.

17. Taylor, SG, Farinholt, KM, Park, G, Farrar, CR, Todd, MD, Lee, JR, Structural health monitoring of research-scale wind turbine blades, Proceedings of the *Asia-Pacific Workshop on Structural Health Monitoring*, Melbourne, Australia, 2012.

18. Berry, D, Design of 9-Meter Carbon-Fiberglass Prototype Blades: CX-100 and TX-100," Sandia National Laboratories Report, Albuquerque, NM SAND2007-0201, 2007

19. Taylor, SG, Farinholt, KF, Choi, M, Jeong, H, Jang, J, Lee, JR, Park, G, Todd, MD, Incipient Crack Detection in Composite Wind Turbine Blades," *Journal of Intelligent Material Systems and Structures*, 2014; 25(5): 613-620.

20. Dervilies, N, Choi, M, Taylor, SG, Barthorpe, RJ, Park, G, Farrar, CR, Worden, K, "On Damage Diagnosis for a Wind Turbine Blade using Auto-Associative Neural Networks," *Journal of Sound and Vibration*, 2014; 333(6): 1833-1850

21. Taylor, SG, Park, G, Farinholt, KF, Todd, MD, Fatigue crack detection performance comparison in a composite wind turbine rotor blade, *International Journal of Structural Health Monitoring*, 2013; 12(3): 252-262.

22. Michaels, JE, Cobb, AC, Michaels, TE, A comparison of feature-based classifiers for ultrasonic structural health monitoring, in *SPIE Smart Stuctures/NDE*, San Diego, CA, 2004, 5394: 363-374.

23. Croxford, AJ, Moll, J, Wilcox, PD, Michaels, JE, Efficient temperature compensation strategies for guided wave structural health monitoring, *Ultrasonics,* 2010; 50(4-5): 517-528.

24. Kay, SM *Fundamentals of Statistical Signal Processing: Detection Theory*. Upper Saddle River, NJ: Prentice-Hall PTR, 1998.

25. Welch, P, The use of fast Fourier transform for the estimation of power spectra: A method based on time averaging over short modified periodograms, *IEEE Transactions on Audio and Electroacoustics,* 1967; 15 (2): 70-73.

26. Vestrand, W, Borozdin, K, Casperson, D, Fenimore, E, Galassi, M, McGowan, K, Starr, D, White, R, Wozniak, P, Wren, J, RAPTOR: Closed Loop monitoring of the night sky and the earliest optical detection of GRB 021211, *Astronomische Nachrichten,* 2004; 325(6): 549-552.

27. Stull, CJ, Taylor, SG, Wren, J, Mascareñas, DL, Farrar, CR, Real-Time Condition Assessment of RAPTOR Telescope Systems, *Journal of Structural Engineering,* 2012: 139(10): 1763-1770.

28. Markel, J, Digital inverse filtering-a new tool for formant trajectory estimation, *IEEE Transactions on Audio and Electroacoustics,* 1972; 20(2): 129-137.